HAL open science

Density fluctuation analysis very near above and below critical point using morphological and spatiotemporal information

Ana Oprisan, Sorinel Oprisan, Yves Garrabos, Carole Lecoutre-Chabot, Daniel Beysens

To cite this version:

Ana Oprisan, Sorinel Oprisan, Yves Garrabos, Carole Lecoutre-Chabot, Daniel Beysens. Density fluctuation analysis very near above and below critical point using morphological and spatiotemporal information. The European Physical Journal Plus, 2021, 136 (5), 523 (17 p.). 10.1140/epjp/s13360-021-01531-8 . hal-03230780

HAL Id: hal-03230780

https://hal.science/hal-03230780v1

Submitted on 21 May 2021

HAL is a multi-disciplinary open access archive for the deposit and dissemination of scientific research documents, whether they are published or not. The documents may come from teaching and research institutions in France or abroad, or from public or private research centers.

L'archive ouverte pluridisciplinaire **HAL**, est destinée au dépôt et à la diffusion de documents scientifiques de niveau recherche, publiés ou non, émanant des établissements d'enseignement et de recherche français ou étrangers, des laboratoires publics ou privés.

THE EUROPEAN PHYSICAL JOURNAL PLUS

Regular Article

Density fluctuation analysis very near above and below critical point using morphological and spatiotemporal information

Ana Oprisan[1,a], **Sorinel A. Oprisan**[1], **Yves Garrabos**[2], **Carole Lecoutre-Chabot**[2], **Daniel Beysens**[3]

[1] Department of Physics and Astronomy, College of Charleston, 66 George Street, Charleston, SC 29424, USA
[2] CNRS, Université de Bordeaux, Bordeaux INP, ICMCB, UMR 5026, F-33600 Pessac, France
[3] Physique et Mécanique des Milieux Hétérogènes, CNRS, ESPCI, PSL Research University, Sorbonne Université, Sorbonne Paris Cité, Paris, France

Received: 8 March 2021 / Accepted: 4 May 2021

Abstract We investigate the fractal nature of critical fluctuations in sulfur hexafluoride (SF_6) under microgravity conditions. For this purpose, we use the Bidimensional Empiric Mode Decomposition (BEMD) approach to separate the spatial scales of fluctuations in orthogonal Independent Mode Functions (IMFs). Statistical analysis of three morphology measures (area, eccentricity, and orientation of convex objects in recorded images) across different IMFs shows that critical fluctuations obey power-laws across multiple spatial scales. We also perform a spatiotemporal analysis of fluctuations by extracting one line of pixels from each image and creating a temporal stack from successive images, or "waterfalls." The spatiotemporal section analysis along the spatial direction reveals multiple spatial scales present in the original fluctuating image. The analysis of the "waterfalls" along the temporal direction identifies a common power-law temporal behavior across all spatial scales. Our results show that critical fluctuations very near critical temperature (T_c) have a fractal structure captured by power-laws with multiple critical exponents. The morphology analysis shows that very near T_c, the fluctuating domains are mostly spherical with some anisotropy.

1 Introduction

Many experiments on the critical behavior of gas-liquid and binary fluids systems have been performed, and they go back to over a hundred years [5,7,9,25,26]. Many of them are light scattering-based experiments [6,35,53,79] that determine thermophysical parameters close to the critical point by relying almost exclusively on Fourier analysis [14,32,58,59]. Fourier transform is a convenient method of switching back and forth between the real physical space (x, y) of the light scattering in the recorded image and the corresponding conjugated space of wavenumbers ($k_x = 2\pi/x, k_y = 2\pi/y$). Compared to the Fourier method, there are only a few studies on direct observation of the scattered light intensity fluctuations in physical space

[a] e-mail: oprisana@cofc.edu (corresponding author)

uncorrected proof

(x, y) of the recorded images [10,23,35,38,39]. Asher and Pankow [2] performed a somewhat similar direct observation of light intensity fluctuations, although they used a laser-induced fluorescence method to measure the timescales of surface concentration fluctuations.

In real space recorded images, light intensity fluctuations appear as domains whose intensity is different from the image's mean intensity. In equilibrium conditions, these fluctuations have large enough sizes to become detectable with optical cameras only when the system is close to criticality. On the other side, non-equilibrium fluctuations become giant thanks to the coupling of spontaneous fluctuations with the existing gradient [77]. This is increasingly true if one removes gravity [75]. The direct imaging of critical fluctuations may answer fundamental questions regarding the correlation between thermal fluctuations and critical percolation points [18,70]. This connection rests on a precise criterion to define clusters that emerge from fluctuations during phase separation, and this up to now is still lacking.

The fluctuations of light intensity $\delta i(x, y)$ detected by light scattering experiments are determined by the corresponding order parameter fluctuations. In pure fluids near their critical point, the order parameter is the reduced critical density, $M = \rho/\rho_c - 1$, where $\rho(\rho_c)$ is the (critical) density of the system.

The signature of self-similarity of the fluctuating domains is the existence of a power-law dependence between the number of the convex areas and their "mass," i.e., the number of pixels in the image belonging to a convex domain [24]. Mathematically, the existence of a scaling equation for an observable $A(r)$, which is a function of a variable r, establishes the quantitative connection between the power-laws and fractals:

$$A(\lambda r) = \lambda^n A(r), \tag{1}$$

where λ is a constant factor and n is a scaling exponent, independent of r [48]. Indeed, a power-law such as $y(r) = \alpha r^n$ is among the functions that obey the above scaling law since $y(\lambda r) = \alpha(\lambda r)^n = \lambda^n y(r)$. The above scaling equation is identical to the recursion formula of the renormalization group theory when recursively integrating the short distance degrees of freedom of the system to generate a sequence of effective Hamiltonians corresponding to increasing scale [47,74,80,81]. The physical quantity $A(r)$ may not be extensive at the critical point due to the long-range correlation of critical fluctuations. As the system approaches a critical point, the asymptotic behavior of the physical quantity $A(r)$ as the length scale changes $L \to L' = L/r$ usually gives a power-law [29,30,73]:

$$A(L') = A(L/r) \propto r^{-\phi} A(L). \tag{2}$$

Near the critical points of phase transition, a new order driven by strong and long-range correlations between dynamic events emerges at all the system's spatial scales. Such a (re)organization of the system occurs at all spatial scales and can be best captured mathematically by power-laws and fractal dimensions [69]. A fluid near its critical point is in constant contact with a thermostat with which it exchanges energy that leads to a coherent macroscopic behavior [17]. Such a process mediated by long-range correlations among fluctuating domains reflects the unity of the physical laws spanning multiple spatiotemporal scales and is captured by scale-free power-law distributions of observables.

The first study that identified an experimental power-law was done by Vilfredo Pareto and modeled the distribution of individuals' incomes, which is called nowadays Pareto law [63]. He found that the relative number of individuals with an annual income larger than a specific value x was proportional to the power of x. Since then, fractal structures characterized by power-law distributions were discovered in the turbulent flow [71], earthquake dynamics

unedited proof

occurrence of an infinite cluster can be associated with the divergence of the fluctuations near the critical point [36].

Our main result is that critical fluctuations very near critical temperature (T_c) have a fractal structure captured by power-laws with multiple critical exponents. Our current approach's advantages are that (1) data analysis is performed in the spatial domain without using Fourier transforms, (2) the image analysis is data-driven, i.e., all measures related to spatiotemporal behavior of the fluctuations are directly related to observed intensity fluctuations, and (3) the BEMD-based analysis is valid even for nonlinear and non-stationary processes.

2 Experimental setup

Images of large thermal fluctuations near the critical point ($T_c = 318.733$ K, $P_c = 37.586$ bar, $\rho_c = 5.0581$ mol l^{-1}) of sulfur hexafluoride (SF_6) in microgravity conditions were recorded using ALICE 2 instruments onboard of 1999 MIR space station [15,28,49,51,55]. In this microgravity experiment, SF_6 above its critical temperature T_c was quenched by quickly decreasing its temperature with steps of 300 μK. Several sets of thermal quenches (see Fig. 1 in [56]) were performed from the one-phase region above critical temperature into the two-phase region below T_c that resulted in phase separation [55,56]. The temperature was monitored with three thermistors placed inside the SCU. For image analysis, we cropped the most extensive possible rectangular area without including data markers. In this paper, we only discuss image processing results based on the last 300 μK thermal quench that stepped through the critical temperature [39,56,60]. The system was prepared at the critical density with the order parameter $M = (\rho - \rho_c)/\rho = 0.0 \pm 0.02\%$. The 300 μK temperature quench through T_c started the phase separation of the fluid (see [39,56,60] for a detailed description of the experimental procedure). Since the phase separation has begun during the last 300 μK thermal quench, we concluded that T_c was somewhere between the upper (UP, i.e., $T > T_c$) and lower (DOWN, i.e., $T < T_c$) plateaus. The exact location of T_c measured from the DOWN plateau was determined with the histogram method to be 46.74 ± 0.03μK [55] and in the range of 15 μK to 42 μK using Dynamic Differential Microscopy (DDM) [56].

The density fluctuations were visualized through light transmission normal to the sapphire windows using a He-Ne laser with 632.8 nm wavelength and about 100 μW maximum power (see also [60] for a detailed description). Laser stability after 1 h was estimated to be better than 0.3 %. An optical microscope of 3.1 μm resolution was also used to record a small SCU region. We used 166 images (6.64 s) recorded for UP ($T > T_c$) plateau. While the first 71 images of the 166 UP series were recorded with the microscope focused on the sapphire window, the rest were recorded with the focal plane at the cell's center. For the DOWN ($T < T_c$) plateau, we used 479 images (19.16 s). All images for the DOWN region were recorded with the focal plane at the center of the cell. The full description of the experiment is presented elsewhere [55,56,60].

3 Methods

3.1 Bidimensional Empiric Mode Decomposition (BEMD)

We use a new data-driven method for multi-scale analysis of critical fluctuations. The method naturally separates the spatial scales based on the image content. The BEMD method breaks the original image into different orthogonal spatial scales called Intrinsic Mode Function

uncorrected proof

(IMF) and one residual quantity [60]. We probe the fractal nature of critical fluctuations by separating spatial scales with the BEMD method followed by (1) morphological analysis and (2) spatiotemporal cross sections ("waterfalls") of all IMFs. For this purpose, the BEMD first separates the fluctuations in orthogonal spatial scales that contrast the morphology and spatial properties more intuitively. We hypothesize that if critical fluctuations have a fractal structure, then morphology measures and spatiotemporal structures should observe similar evolutions across all spatial scales represented by individual IMFs.

In the past, the Empirical Mode Decomposition (EMD) has been applied to earthquake analysis [41,64], structural diagnosis [31,52], characterization of non-stationary biological processes [44], mechanical fault diagnosis [84,85], and ocean waves analysis [72]. One advantage of EMD over traditional spectral analysis methods is that it can be applied even to nonlinear and non-stationary signals and produces linear and stationary IMFs [43]. Intuitively, the EMD is a data-driven adaptive method that allows recursive removal of oscillations (IMFs) by repeated subtraction of an appropriately defined baseline [34,40–44]. For two-dimensional data sets (images), we used a BEMD algorithm [65] that requires no pre-determined filter or wavelet function [68]. The BEMD has been applied to texture extraction and image filtering [45], finding the gold mineral deposition [40], the discovery of tin-copper polymetallic ore field [16] by gravity anomalies captured by satellite images, image denoising [4,50], content-based image retrieval [1], and fusion of multispectral and remote sensing [27,34,37]. We recently expanded the application of the BEMD method and combined it with the Dynamic Differential Microscopy (DDM) to the analyses of critical fluctuations [60]. All the details of decomposing fluctuation images based on BEMD are described in [60]. BEMD is a fully adaptive multi-scale decomposition because it operates on the local extremum sequence. The decomposition is carried out by direct extraction of the local energy associated with the signal itself's intrinsic time-scales. This approach is different from the wavelet-based multi-scale analysis that characterizes the scale of a signal event using pre-specified basis functions [82].

For this study, we only considered three IMFs, plus the residual image [60]. Representative examples of the original images, their first three IMFs, and the residual are shown in Fig. 1. The BEMD decomposition contains the fluctuations from finest to coarsest spatial scale. Since the sifting process extracts from the original image (Fig. 1A1 and A2) first the highest spatial frequency (Fig. 1B1 and B2), the first IMF mode corresponds to the short-range fluctuations, which we expect to dominate very close to the critical point. Conversely, the image tendency and the long-range correlations of fluctuations are contained in the next two modes (Fig. 1C1-C2 and D1-D2). The residue (Fig. 1E1 and E2) represents the largest spatial scale of fluctuations obtained from the data. The residual is usually used as a background image to correct for nonuniform illumination.

3.2 Spatiotemporal cross sections

The spatiotemporal correlations of fluctuations could be captured with the stacked one-dimensional sections through individual images, i.e., "waterfalls" [39]. For this purpose, a horizontal line of pixels was extracted from successive images at the same location, which gave the spatial dimension of the image, called "space" in Fig. 2A1. The rows of pixels (one row from each recorded image) were stacked according to the image index (time) along the vertical direction, which gave the temporal dimension called "time" in (see Fig. 2)A1.

To obtain the original spatiotemporal ("waterfall)" images, we first applied the BEMD decomposition to the original images, as shown in Fig. 1. Subsequently, we created for each IMF order the corresponding spatiotemporal ("waterfall") image as described above and shown in Fig. 2A1-A4. An optimum gray-level threshold was selected for each line of pixels,

Uncorrected Proof

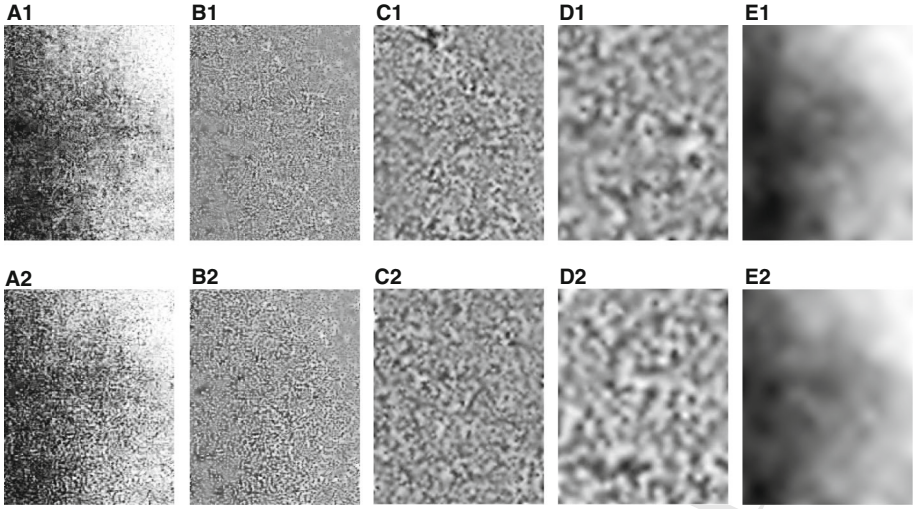

Fig. 1 The original images (A1 above T_c (UP with cell centered focus) and A2 below T_c (DOWN with cell centered focus)), the first three IMFs (B1-D1 for UP and B2-D2 for DOWN), and the residual image (E1 for UP and E2 for DOWN) for the image index 100 of UP and the image index 200 of DOWN region. Above critical temperature (panels A1-E1), the finest spatial scale (B1) shows small size fluctuations, which correspond to the fluctuations' finest spatial scale. For the DOWN region (B2), the first IMF's characteristic spatial distance seems to be comparable to UP, which is consistent with the early stage phase separation processes. The coarse spatial scales (C and D) show long-range correlation patterns of fluctuations. The residue (E) has a structure that suggests a long-range correlation of fluctuations

and the "waterfalls" were converted to black and white images (see Fig. 2B1-B4). We chose one threshold per line instead of a single threshold for the entire "waterfall" image because each line belongs to a different fluctuation image. This way, each line of pixels is thresholded based on the correct context it belongs to, i.e., its original image. To binarize the original grayscale images, we computed for each image a threshold based on Otsu's method [62]. Otsu's method chooses a threshold that minimizes the intraclass variance of the thresholded black and white pixels. Although we only show in Fig. 2 the stack of rows through the middle of each image, we repeated the same procedure at 25 % and 75 % of image height and found no statistical difference with the results presented here for the central line of pixels. A similar approach was used for the DOWN region. The black and white thresholded grayscale images were used for edge detection of convex objects during morphology analysis.

4 Results

4.1 Morphological analysis of critical fluctuations

We used an in-house Matlab code to compute a set of properties specified by the 8-connected component (object) in the binarized fluctuation images (see Fig. 3B). In a two-dimensional image on a rectangular lattice, any given pixel is connected with eight adjacent pixels if their edges or corners touch, as shown in Fig. 3A. Two adjoining pixels are part of the same object if they are both on and are connected along the horizontal, vertical, or diagonal direction (see Fig. 3A for an 8-connected central pixel). Out of the 25 different properties computed,

Uncorrected

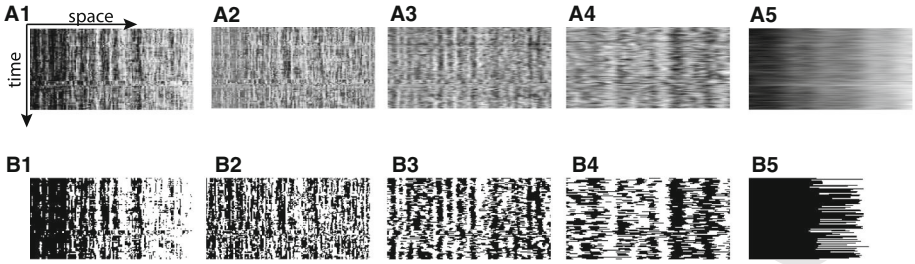

Fig. 2 Stacks of one-dimensional sections through the center of each fluctuation image of the UP region. The original (A1) grayscale images were separated into three IMFs plus a residual image using the BEMD algorithm (A2-A5). The shortest spatial scale is contained in A2 and the longest in A5. The corresponding thresholded black and white images (B1-B5) allow a clear identification of the boundaries of convex domains (black pixels)

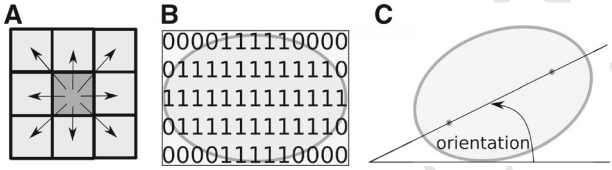

Fig. 3 (A) In two-dimensional images, an 8-connected central pixel has similar pixels along edges or corners. Two adjoining pixels are part of the same object if they are both on and are connected along the horizontal, vertical, or diagonal direction. (B) The eccentricity of a morphological object is the ratio of the distance between the foci of the ellipse and its major axis length. The value is between 0 (circle) and 1 (line segment). (C) The orientation of an elliptical object is given by the angle between the x-axis and the major axis of the ellipse. The value is in degrees, ranging from $-90°$ to $90°$. The two dots on the major axis represent the foci of the ellipse

we only present the statistics of the three most relevant measures for the morphology of fluctuations, i.e., area, eccentricity (see Fig. 3B), and orientation (see Fig. 3C).

At least 40 % of the compact, i.e., convex, objects with clear boundaries have an area of one arbitrary unit (see Fig. 4A1-B1 for the original image, A2-B2 for IMF1, and A3-B3 for IMF2). As expected, large objects are scarce, reflected by a power-law decay of the percentage of compact objects' area versus their size (see Fig. 4A1-B1 for the original images). The statistics of only three representative images are shown in Fig. 4A1-A3 and B1-B3, respectively. The slope of the log-log plots shown in Fig. 4 represents the power-law exponents. The UP region has the first 71 images recorded with the focal plane of the microscope on the sapphire window of the SCU and the rest with the focal plane at the center of the SCU. The statistical analysis was performed separately for the two subsets of images recorded above T_c. Our statistical analysis of the morphology of fluctuation using convex area measure revealed no statistically significant difference between the 71 images and the rest for the UP region (see Fig. 4). As a result, the subsequent statistical analysis for other morphological measures (eccentricity and orientation) lumped together the two subsets of the UP dataset. From the UP region images recorded with the focal plane at the center of the SCU (Fig. 4A1-A3) and from the DOWN region (Fig. 4B1-B3), we only show the log-log plots for a set of three images selected at the beginning of the set, in the middle, and at the end of the respective dataset.

We fitted all area distributions for every image with power-laws given by $\%objects \propto area^n$, where the exponent values n are shown in Fig. 5A1-A2 for all images and their IMFs.

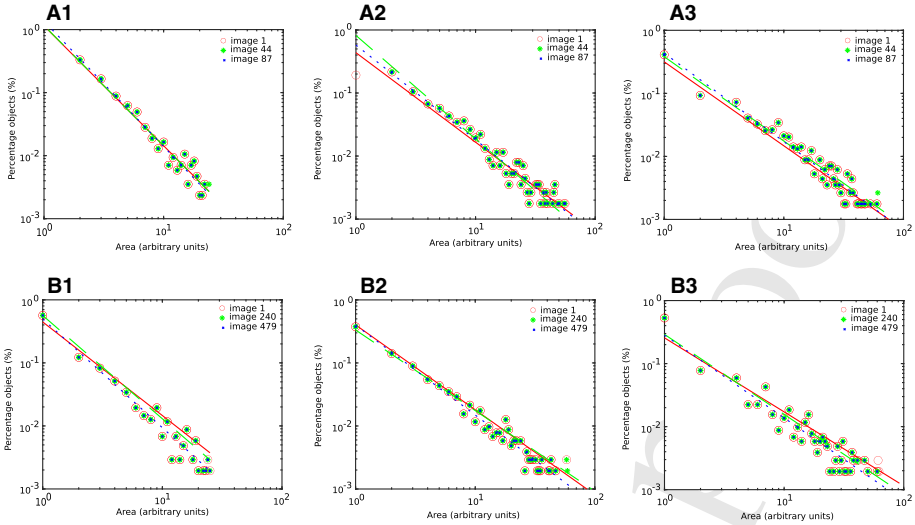

Fig. 4 The distribution of the area of the convex objects identified in fluctuations images. The top panels are for the original images (A1) and the first two IMFs (A2 and A3) of the UP region ($T > T_c$) with the focal plane in the center of the SCU. The bottom panels (B1-B3) correspond to the DOWN region ($T < T_c$) with the focal plane in the center of the SCU. The panels A1-B1 represent the original images, the panels A2-B2 represent the first IMF, and A3-B3 correspond to the second IMF. For each region UP/DOWN, we selected only three images

The area distributions of the third and fourth IMF are not shown, but a numerical summary is presented in Table 1. A summary of the UP plateau's power-law exponents is shown in Fig. 5A1, where the window- and center-focused data are separated by a vertical dashed line. Although we monitored multiple measures of the goodness of fit, e.g., the sum of squared error, the root mean square error, we only show in Fig. 5B1-B2 the adjusted R^2 coefficient as a measure of the goodness of fit. Adjusted $R^2 \in [-1, +1]$ determines the extent of the dependent variable's variance, which the independent variable can explain. The higher the adjusted R^2, the better the regression equation captures the dependent variable's variance by the chosen independent variable(s). The average adjusted R^2 coefficient was over 92 % for the original images and the first IMF and over 87 % for IMF2. From Fig. 5A1, we notice a significant variance of the power-law exponent for the first 71 images of the UP plateau than the rest of the recording. Since the mean values across all original and IMFs are consistent and statistically identical both for the first 71 images recorded with the window focus and the rest of the images of the UP plateau recorded with the focus plane at the center of the SCU, the observed larger variance for the first subset is not due to the location of the focal plane. A possible explanation for the observed variability is that the first 71 images are recorded closer to when the thermal quench was applied and related to transient phenomena during thermal equilibration. An alternative explanation could reside in the fact that the proximity to the cell border alters the critical fluctuations due to the presence of preferential adsorption on lengthscale ξ (see [8,83] and references therein).

The vertical dashed line in Fig. 5A1 separates the first 71 images of the UP dataset recorded with the focal plane on the sapphire window from the images recorded with the focal plane at SCU center.

Accepted Proof

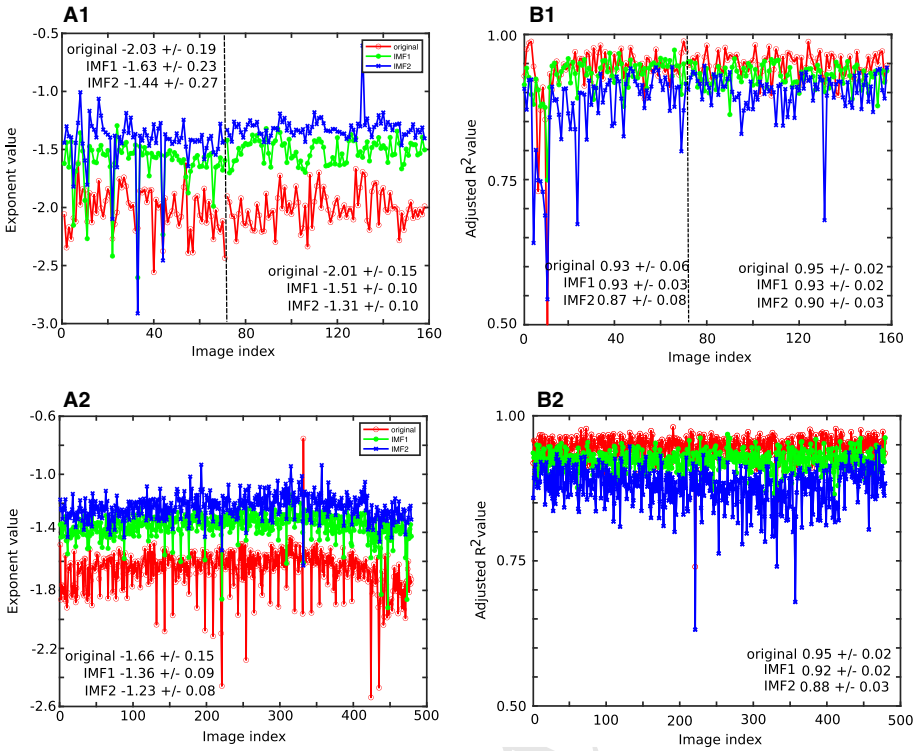

Fig. 5 Power-law exponents and the goodness of fit. Panel A1 (A2) shows the power-law exponents that best fitted the area distributions in the original image (empty red circles), IMF1 (solid green circles), IMF2 (blue "x" marks) for the UP (DOWN) region. The panels B1 and B2 represent the respective goodness of fit measured by the adjusted R^2 value. The mean values (and the standard deviations) of the power-law exponents (panels A1 and A2) decrease in absolute value from the original images to IMF1 and IMF2. The mean value of the adjusted R^2 also decreases from 95 % for the original images to 92 %-93 % for IMF1 and 88 %-90 % for IMF2. All mean values are given with the corresponding standard deviations

Table 1 Power-law exponents extracted from the log-log plot of the area distributions shown in Fig. 4

	original	IMF1	IMF2	IMF3	IMF4
UP window	-2.03 ± 0.19	-1.63 ± 0.23	-1.44 ± 0.27	-1.51 ± 0.29	-1.49 ± 0.29
UP center	-2.01 ± 0.15	-1.51 ± 0.10	-1.31 ± 0.10	-1.36 ± 0.05	-1.35 ± 0.05
DOWN	-1.66 ± 0.15	-1.36 ± 0.09	-1.23 ± 0.08	-1.26 ± 0.07	-1.25 ± 0.07

Despite large variabilities and some obvious outliers in the power-low fitting exponents shown in Fig. 4A4-B4, the trends are quite stable. We notice first that the mean values and standard deviations for the first 71 images of the UP region recorded with the focal plane on the sapphire window are within the standard deviation of the next set of images recorded with the focal plane at the center of the SCU (see Table 1). This result has two consequences: 1) supports the ergodic hypothesis that fluctuations have the same structure regardless the focal plane of recordings, and 2) allows us to lump together the first 71 images recorded with the focal plane on the sapphire window with the rest of the UP images recorded with the focal plane at the center of the SCU.

uncorrected

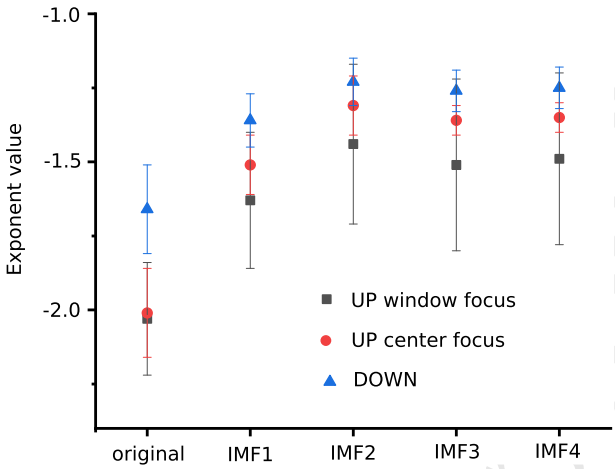

Fig. 6 Mean and standard deviation plots of the power-law exponents for array distributions shown in Fig. 4. The original images gave the largest (in absolute value) exponents with a steady decrease (in absolute value) for IMF1 and IMF2. The exponents for IMF3 and IMF4 are statistically similar, although the actual images are significantly different (see Fig. 1D for IMF3 and Fig. 1E for IMF4). For the UP region, the exponents obtained with the microscope focused on the sapphire window (solid black squares) are statistically identical to those for the microscope focused at the center of the cell (solid red circles). For the DOWN region, the exponents are significantly smaller (in absolute value) compared to UP region (see solid blue triangles

The average exponents that summarize Fig. 4 are given in Table 1 and the corresponding Fig. 6. As expected, the distribution of areas in the original images (Fig. 4A1-B1) has the smoothest decay and the largest (absolute value) exponent in Table 1 because they contain all IMFs.

The fact that the exponents for the original images and the first two IMFS are statistically different suggests that the smoothness of quantitative measures associated with original images could be misleading because it lumps together processes on different spatial and temporal scales. The similar values of the exponents for IMF3 and IMF4 suggest that, although the actual images look different, the area measure is not sensitive enough to distinguish between these two IMFs. This is because both IMF3 and IMF4 contain the largest spatial scales of the original images, and they do not contain significantly different small-scale convex objects to tilt the array distribution toward one of the two IMFs.

Since the original images include convex objects across all spatial scales, they will be separated and smoothened by the BEMD image processing when computing IMF1. As a result, the power-law exponents for IMF1 will reflect the smoothing effect of the BEMD algorithm leading to a smaller (in absolute value) exponent compared to the original image. This is because BEMD smoothing of fast spatial oscillations in the original images will spread the spatial scale over a wider range of sizes. A similar explanation is valid for IMF2. The saturation and plateau observed for the exponents across IMF2, IMF3, and IMF4 (see Fig. 6) suggests that we may not have more than two spatial and temporal scales present in our original image. As a result, adding higher-order IMFs does not add significant new information to our analysis. Therefore, in the subsequent statistical analysis, we will drop the last IMF4 as it does not add significantly more information than IMF3.

The eccentricity of convex objects in analyzed images indicates possible anisotropy induced by nucleation [66,67], coalescence-induced coalescence [11,46,54], dimple coalescence [11,57], and other processes that lead to phase separation. The eccentricity of the

Proof

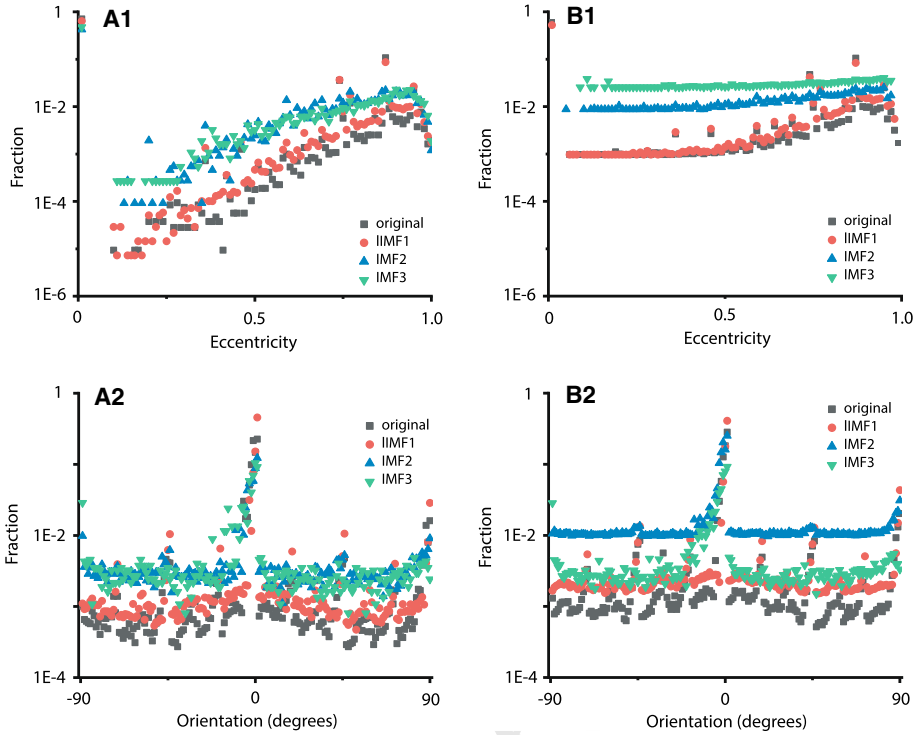

Fig. 7 The eccentricities and orientations of convex areas in fluctuation images. In both UP (left panels A1) and DOWN (right panels B1) regions, the zero-eccentricity (circular cross section) dominates the identified convex objects with larger eccentricities not exceeding 1 % of the total objects identified. The orientations of the elliptical areas are dominated by zero degrees (circles plus some ellipses), and the contribution of other orientations is also less than 1 % (A2 for UP and B2 for DOWN, respectively). All plots are on the semilogarithmic axis to emphasize that nonzero contribution for eccentricity and orientation is tiny

convex objects identified in fluctuation images is measured as the ratio of the distance between the foci of the ellipse and its major axis length (see Fig. 3B). The value of eccentricity is between 0 (circle) and 1 (a line segment). We show the eccentricity on the semilogarithmic axis (see Fig. 7A1 for UP and Fig. 7B1 for DOWN) to emphasize that although objects with nonzero eccentricity were identified in images, their fraction is very small. Indeed, in all original images and the first three IMFs, the largest percentage of objects are circular (no eccentricity), whereas the largest nonzero eccentricity fraction is around 1 %. We summarized in Table 2 the percentage of circular objects identified in the original images and their IMFs. The fact that about 70 % of objects have a circular shape in the UP region aligns with our hypothesis that above the critical point, we only expect short-range correlations that lead to spherical (circular cross section) objects in the absence of any gradients. The fact that over 60 % of objects have a circular shape in the DOWN region indicates that, although the fluctuations are more anisotropic below T_c, the fluid is still very close to T_c in the early stage of phase separation. This suggests that a few tens of μK around T_c, the local field is still pretty uniform, and there is no significant hydrodynamic anisotropy, such as those induced by coalescence-induced coalescence or dimple coalescence [39,56].

Another measure of the system's anisotropy is the orientation of the convex objects in the fluctuation images (see Fig. 3C). We measured the angle between the x-axis and the major axis

Table 2 The percentage of objects with zero eccentricity in Fig. 7A1-B1

	original	IMF1	IMF2	IMF3
UP	71 ± 11	64 ± 13	43 ± 16	48 ± 18
DOWN	60 ± 6	52 ± 6	39 ± 11	45 ± 14

of the elliptical areas identified in fluctuation images, ranging from $-90°$ to $90°$. For spherical objects, the algorithm selects the major axis along the x-direction, i.e., 0° orientation. We found that the 0° orientation of convex areas dominates the distribution of orientations. In other words, all zero eccentricity objects (circular cross-section) plus some ellipses that may have 0° orientation (see Fig. 7A2-B2) dominate critical fluctuations very near T_c. We used the semilogarithmic axis again to emphasize that the contribution of orientations other than 0° is below 1 %. The very low eccentricity combined with the high ratio of 0° orientation suggests that the fluctuation patterns are relatively homogeneous and mostly spherical very near above and below T_c.

4.2 Spatiotemporal cross sections

The phase separation dynamics that take place near T_c could be captured by the spatiotemporal "waterfalls," i.e., temporal stacks of single-pixel lines. The morphological properties identified in the previous section only capture a few features of critical fluctuations very near above and below the critical temperature.

We determined the distribution of contiguous black pixels along the horizontal (spatial) direction of "waterfalls" shown in Fig. 2. Such a distribution gives information about the spatial size of fluctuations and is shown in Fig. 8A1-A2. For all microscopic images, the 1 pixel = 3.1 μm. The "waterfall"'s spatial dimension statistics contain different information than the distribution of the areas of convex objects identified through morphology analysis. In the spatiotemporal images (see Fig. 2), we analyze the evolution of contiguous linear domains at the same location across all original images and their IMFs. While it is possible for a cross section of an image to contain the same information about the statistics of fluctuations as the whole image, such an ergodic assumption is only valid in the limit of a very large cross section. Due to the finite size of the cross section, i.e., a one-pixel line from each image, we expect slightly different power-law exponents for the spatiotemporal cross sections compared to the morphology analysis.

All spatial distributions for all original images and their IMFs have the same general structure: they monotonically increase to a peak and then decay as a power-law (shown as straight-line patterns in a log-log plot of Fig. 8A1-A2). We fitted the spatial distribution data with a power-law over an adjustable range of distances that gave us the best goodness of fit with the maximum possible coefficient of determination. For example, for the original image in Fig. 8A1, the best range was 3 to 24 pixels; for IMF1, the range was 4 to 20 pixels; for IMF2 was 6 to 29 pixels, and for IMF3, it was 14 to 52 pixels.

There are similarities between the spatiotemporal statistics (Table 3) and convex area statistics from morphology analysis (Table 1). In both cases, the power-law exponents increase from the original images as the IMF order increases. Such consistent behavior supports the ergodic hypothesis, i.e., the dynamics of fluctuations is the same whether we analyze the whole image using morphology measures or only a cross section as in the case of "waterfalls." The second conclusion from the power-law exponents' consistent trend is that the fractal hypothesis is supported by the existence of power-laws holds across all IMFs. We noticed

Uncorrected Proof

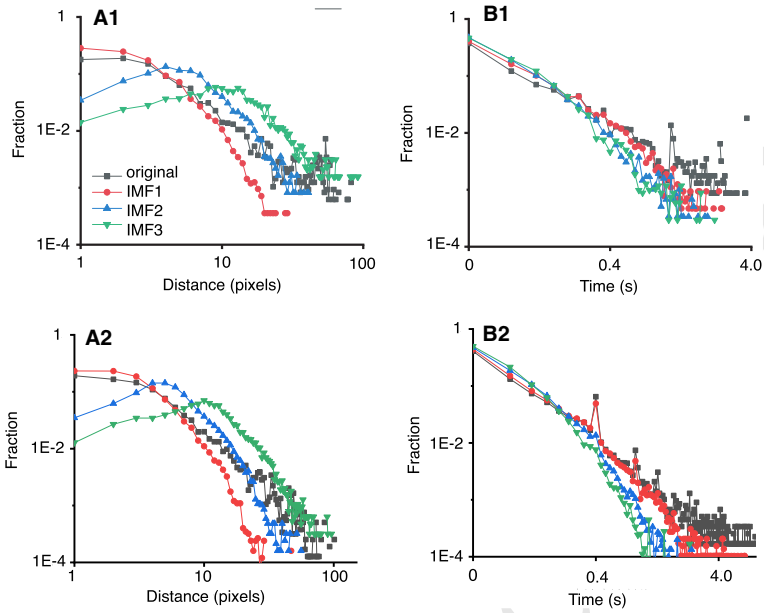

Fig. 8 Distributions of spatial (A1-A2) and temporal (B1-B2) fluctuation sizes. The spatial size of fluctuations has a peak that depends on the IMF's spatial scale (A1 for UP and A2 for DOWN). Spatial unit is 1 pixel = 3.1 μm. After the peak, all distributions decay as power laws with quite close exponents (see Table 4). The distribution of temporal correlations for all IMFs follows identical patterns with two different exponents: a relatively small exponent for durations shorter than 0.4 s and a much more negative exponent for longer correlation times (B1 for UP and B2 for DOWN). There were 25 frames per second

Table 3 The power law exponent of spatial distribution of objects in Fig. 8A1-A2. The distances are measured in pixels with 1 pixel = 3.1 μm

	original	IMF1	IMF2	IMF3
UP	-1.75 ± 0.04	-2.19 ± 0.08	-2.30 ± 0.07	-2.4 ± 0.1
DOWN	-0.93 ± 0.05	-0.94 ± 0.10	-2.50 ± 0.05	-2.45 ± 0.06

in both the morphology analysis (Table 1) and the spatiotemporal cross sections (Table 3) that the exponents of the original images and IMF1 are very close, which suggests that the critical fluctuations are captured for the most part by the finest spatial scale of IMF1.

There are also differences between UP and DOWN plateaus revealed by spatial statistics. For example, the power-law exponents of spatiotemporal cross sections for both the original and IMF1 in the UP region are about twice as large as the exponents for the DOWN region (Table 3). This shows that, although the fractal nature of fluctuations revealed by the power-laws is preserved, the DOWN region has a much smoother distribution of linear sizes. Another significant difference is that the power-law exponent increases from the original image to IMF1 only for the UP region (Table 1 and (Table 3), whereas for DOWN, the exponents are almost constant. This means that below T_c, both the original and IMF1 have similar spatial dynamics.

The distribution of temporal correlations measured along the temporal axis (vertical) direction has completely different dynamics than the spatial correlation, as shown in Fig. 8B1-

Table 4 The power-law exponent of temporal distribution from Fig. 8B1-B2

	original	IMF1	IMF2	IMF3
UP ($t < 0.4$ s)	-1.44 ± 0.04	-1.48 ± 0.02	-1.32 ± 0.03	-1.41 ± 0.08
UP ($t > 0.4$ s)	-1.6 ± 0.1	-2.5 ± 0.3	-3.2 ± 0.4	-2.4 ± 0.3
DOWN ($t < 0.4$ s)	-1.42 ± 0.03	-1.39 ± 0.03	-1.33 ± 0.04	-1.39 ± 0.06
DOWN ($t > 0.4$ s)	-1.7 ± 0.12	-2.26 ± 0.10	-3.5 ± 0.2	-3.0 ± 0.4

B2. All IMFs have almost the same power-law distribution up to 0.4 s (the equivalent of 10 video frames), and then the power-low exponent drops significantly (see Fig. 8B1-B2 and Table 4). The fact that there are two different exponents for the temporal correlation suggests that indeed the correlation time of fluctuations is best described by a double exponential [39,55,56]. The difference in the two exponents is clear when comparing the fitting for short durations $t < 0.4$ s against longer durations with $t > 0.4$ s for all IMFs (see Fig. 8B1-B2 and Table 4). The temporal correlation exponent (Table 4) for short durations (below 0.4 s) is statistically identical both for the UP and the DOWN regions. Moreover, the exponents are almost constant across the original images and their IMFs. This suggests that fluctuations in the temporal statistics are not sensitive to spatial scale separation performed with the BEMD. The characteristic times of fluctuations decrease as $t^{-1.4}$ for the original images.

For longer correlation times (above 0.4 s), the distribution scales as $t^{-1.7}$ and is no longer invariant to BEMD spatial decomposition. The increase in the power-law exponents with the IMF order indicates that larger fluctuations lose temporal correlation much faster than smaller clusters. As expected, the original image's power-law exponents do not show such a large discontinuity because it lumps together multiple spatial and temporal scales (see Table 4). For this reason, in the DDM analysis of fluctuation images the correlation time of fluctuations is represented by a single power-law exponent [3,19–21,33,61,75,76].

5 Conclusions

The recent extension of the classical theory of fluctuations to non-equilibrium processes [76] showed that the temporal correlation of fluctuations could be directly obtained from fluctuation images. It can lead to experimental advances in measuring diffusion and viscosity coefficients. The information regarding the evolution and the scaling of the fluctuation correlation time is contained in the Intermediate Scattering Function (ISF). For pure fluid in thermal equilibrium, the ISF is a Gaussian with width proportional to the diffusion time. There are cases when ISF contains multiple time scales, and one approach for mitigating this issue has been the fitting of ISF with multiple exponentials to capture each characteristic time separately [3,61]. This approach allowed, for example, the separation of the thermal diffusivity coefficient from the mass diffusivity [3].

Instead of investigating the fluctuations in Fourier space through their ISFs, we here carried out a direct space analysis of fluctuations. For this purpose, we used the BEMD, data-driven technique to decompose the spatial frequency components into an orthogonal set of Intrinsic Mode Function (IMFs). This method is suitable for analyzing nonlinear and non-stationary data, such as the thermal quench data that stepped through the critical temperature T_c in our microgravity experiment.

Uncorrected Proof

Different physical processes act over different spatial and temporal ranges. Very near the critical point of a phase transition, dynamical fluctuations reach macroscopic magnitude and overrule molecular size, shape, and interactions in dictating bulk behavior [22,78]. These fluctuations are generated by the nonlinear dynamics of classical critical fluids. Recent large-scale numerical simulations showed that when approaching the liquid-vapor critical point from the supercritical regime, $T > T_c$, the Lyapunov exponents associated with the phase space dynamics of molecules decrease monotonically [22]. This is due to the fact that critical fluctuations imply structural organization as opposed to molecular chaos and dynamic instability. The Lyapunov exponents measure how quickly infinitesimally closed phase space points separate over time. Large Lyapunov exponents indicate more unstable phases space dynamics. As the system approaches T_c from above, the divergence of trajectories "slows down" and allows the formation of spatial regions in the system that will separate into coexisting vapor and liquid phases below T_c.

We found consistent power-laws across all spatial scales, which supports our hypothesis of critical fluctuations' fractal nature. The morphology analysis showed that very near T_c, the fluctuating domains are mostly spherical with some anisotropy. Spatiotemporal cross sections showed that the distribution of contiguous domains also obeys free-scale power-laws near T_c that support the fractal hypothesis of critical fluctuations. The temporal correlation of fluctuations also follows a power-law with the same exponent across all spatial scales (for correlation times shorter than 0.4 s (10 video frames). This surprising result supports the hypothesis of a "slowing down" in the divergence of molecular trajectories [22] across all spatial scales to allow phase separation.

Acknowledgements AO and SAO acknowledge 2020-2021 Mini-Research and Education Awards Program and Palmetto Academy grants from South Carolina Space Grant/EPSCoR in support for this research. SAO acknowledges a 2020-2021 Research and Development grant from the College of Charleston. YG, CL and DB. acknowledge a research grant from Centre National d'Études Spatiales (CNES) and a NASA grants NAG3-1906 and NAG3-2447.

Author contributions AO and SAO perform image and statistical analysis. YG, CL, and DB conducted the microgravity experiments and contributed to data analysis. All authors wrote the paper together and approved the final manuscript.

References

1. P.F. Alvanitopoulos, A. Moroi, G. Bagropoulos, K. Dundon, Content Based Image Retrieval and Its Application to Product Recognition, in *Artificial Intelligence Applications and Innovations*. ed. by R. Chbeir, Y. Manolopoulos, I. Maglogiannis, R. Alhajj. pp. (Springer International Publishing, Cham, 2015), pp. 3–18
2. W. Asher, J.F. Pankow, Direct observation of concentration fluctuations close to a gas-liquid interface. Chem. Eng. Sci. **44**(6), 1451–1455 (1989)
3. H. Bataller, C. Giraudet, F. Croccolo, and J. Maria Ortiz de Zarate. Analysis of Non-Equilibrium Fluctuations in a Ternary Liquid Mixture. *Microgravity Science and Technology*, 28, 2016
4. F. Ben Arfia, A. Sabri, M. Ben Messaoud, and M. Abid. The bidimensional empirical mode decomposition with 2D-DWT for gaussian image denoising. In *2011 17th International Conference on Digital Signal Processing (DSP)*, pages 1–5, 2011
5. Bertrand Berche, Malte Henkel, and Ralph Kenna. Critical phenomena: 150 years since cagniard de la tour. *Revista Brasileira de Ensino de FÃsica*, 31:2602.1 – 2602.4, 06 2009
6. B.J. Berne, R. Pecora, *Dynamic Light Scattering: With Applications to Chemistry, Biology, and Physics Dover Books on Physics Series* (Dover Publications, New York, 2000)
7. D. Beysens. Critical Phenomena. *Materials Sciences in Space, a Contribution to the Scientific Basis of Space Processing*, page 191, 1986

uncorrected proof

8. D. Beysens, D. Estève, Adsorption phenomena at the surface of silica spheres in a binary liquid mixture. Phys. Rev. Lett. **54**, 2123–2126 (1985)
9. D. Beysens, M. Gbadamassi, L. Boyer, Light-scattering study of a critical mixture with shear flow. Phys. Rev. Lett. **43**, 1253–1256 (1979)
10. D. Beysens, P. Guenoun, and F. Perrot. Direct observation of critical fluctuations. *Journal of Physics: Condensed Matter*, 2:SA127–SA133, 1990
11. A. Daniel, Beysens, Kinetics and morphology of phase separation in fluids: The role of droplet coalescence. Phys. A: Stat Mech Appl **239**(1), 329–339 (1997)
12. Juan Camilo Bohorquez, Sean Gourley, Alexander R. Dixon, Michael Spagat, and Neil F. Johnson. Common ecology quantifies human insurgency. *Nature*, 462:911–914, 2009
13. J.M. Carlson, J.S. Langer, Mechanical model of an earthquake fault. Phys. Rev. A **40**, 6470–6484 (1989)
14. R. Cerbino, A. Vailati, Near-field scattering techniques: Novel instrumentation and results from time and spatially resolved investigations of soft matter systems. Curr. Opin Coll Interface Sci. **14**(6), 416–425 (2009)
15. L. Chen, *Handbook of Research on Advancements in Supercritical Fluids Applications for Sustainable Energy Systems Advances in Chemical and Materials Engineering* (IGI Global, Hershey, 2020)
16. Y.Q. Chen, L.N. Zhang, B.B. Zhao, Application of Bi-dimensional empirical mode decomposition (BEMD) modeling for extracting gravity anomaly indicating the ore-controlling geological architectures and granites in the gejiu tin-copper polymetallic ore field, southwestern china. Ore Geol. Rev. **88**, 832–840 (2017)
17. Aaron Clauset, Cosma Rohilla Shalizi, and M. E. J. Newman. Power-law distributions in empirical data. *SIAM Review*, 51(4):661-703, Nov 2009
18. Antonio Coniglio. Percolation and critical points. *Journal of Physics: Condensed Matter*, 13(41):9039–9053, sep 2001
19. F. Croccolo. *Dynamics of Non Equilibrium Fluctuations in Free Diffusion*. Thesis, 2006
20. F. Croccolo, D. Brogioli, A. Vailati, M. Giglio, D.S. Cannell, Use of dynamic schlieren interferometry to study fluctuations during free diffusion. Appl. Opt. **45**(10), 2166–2173 (2006)
21. F. Croccolo, C. Giraudet, H. Bataller, R. Cerbino, A. Vailati, Shadowgraph analysis of non-equilibrium fluctuations for measuring transport properties in microgravity in the GRADFLEX experiment. Microgravity Sci. Technol. **28**(4), 467–475 (2016)
22. M. Das, J.R. Green, Critical fluctuations and slowing down of chaos. Nat. Commun. **10**, 2155 (2019)
23. P. Debye, R.T. Jacobsen, Direct visual observation of concentration fluctuations in a critical mixture. J. Chem. Phys. **48**(1), 203–206 (1968)
24. L.A. Dissado, R.M. Hill, Self-similarity as a fundamental feature of the regression of fluctuations. Chem. Phys. **111**(2), 193–207 (1987)
25. C. Domb, Critical phenomena: a brief historical survey. Contemporary Phys. **26**(1), 49–72 (1985)
26. C. Domb, *The Critical Point: A Historical Introduction to the Modern Theory of Critical Phenomena* (CRC Press, Florida, 1996)
27. W. Dong, X. Li, X. Lin, and Z. Li. A Bidimensional Empirical Mode Decomposition Method for Fusion of Multispectral and Panchromatic Remote Sensing Images. *Remote Sensing*, 6:8446–8467, 09 2014
28. Alain Durieux and Isabelle Petitbon. ALICE: optical instrument for observation, interferometry, and diffusion of critical fluids in microgravity. In Thierry M. Dewandre, Joachim J. Schulte in-den Baeumen, and Emmanuel Sein, editors, *Space Optics 1994: Space Instrumentation and Spacecraft Optics*, volume 2210, pages 249 – 258. International Society for Optics and Photonics, SPIE, 1994
29. E. Michael, Fisher, Helen Au-Yang, Critical wall perturbations and a local free energy functional. Phys. A: Stat. Mech. Appl. **101**(1), 255–264 (1980)
30. Michael E. Fisher, Michael N. Barber, Scaling theory for finite-size effects in the critical region. Phys. Rev. Lett. **28**, 1516–1519 (1972)
31. A. Garcia-Perez, J.P. Amezquita-Sanchez, A. Dominguez-Gonzalez, R. Sedaghati, R. Osornio-Rios, R.J. Romero-Troncoso, Fused empirical mode decomposition and wavelets for locating combined damage in a truss-type structure through vibration analysis. J. Zhejiang Univ. Science A **14**(9), 615–630 (2013)
32. F. Giavazzi, D. Brogioli, V. Trappe, T. Bellini, R. Cerbino, Scattering information obtained by optical microscopy: Differential dynamic microscopy and beyond. Phys. Rev. E **80**, 031403 (2009)
33. F. Giavazzi, A. Fornasieri, A. Vailati, R. Cerbino, Equilibrium and non-equilibrium concentration fluctuations in a critical binary mixture. Europ. Physi. J. E **39**(10), 103 (2016)
34. L. Guang, L. Li, H. Gong, Q. Jin, X. Li, R. Song, Y. Chen, Y. Chen, C. He, Y. Huang, Y. Yao, Multisource remote sensing imagery fusion scheme based on bidimensional empirical mode decomposition (BEMD) and its application to the extraction of bamboo forest. Remote Sens. **9**, 19 (2016)
35. P. Guenoun, R. Gastaud, F. Perrot, D. Beysens, Spinodal decomposition patterns in an isodensity critical binary fluid: Direct-visualization and light-scattering analyses. Phys. Rev. A **36**(10), 4876 (1987)

Uncorrected Proof

36. P. Guenoun, F. Perrot, D. Beysens, Microscopic observation of order-parameter fluctuations in critical binary fluids: Morphology, self-similarity, and fractal dimension. Phys. Rev. Lett. **63**(11), 1152 (1989)
37. Z. He, Q. Wang, Y. Shen, J. Jin, Y. Wang, Multivariate gray model-based bemd for hyperspectral image classification. IEEE Trans. Instrum. Measure. **62**(5), 889–904 (2013)
38. J. Hegseth, A. Oprisan, Y. Garrabos, V.S. Nikolayev, C. Lecoutre-Chabot, D. Beysens, Wetting film dynamics during evaporation under weightlessness in a near-critical fluid. Phys. Rev. E **72**(3), 031602 (2005)
39. J.J. Hegseth, A. Oprisan, Y. Garrabos, D. Beysens, Imaging critical fluctuations of pure fluids and binary mixtures. Phys. Rev. E **90**, 022127 (2014)
40. J. Huang, B. Zhao, Y. Chen, P. Zhao, Bidimensional empirical mode decomposition (BEMD) for extraction of gravity anomalies associated with gold mineralization in the tongshi gold field, western shandong uplifted block, eastern china. Comput. Geosci. **36**(7), 987–995 (2010)
41. J.-Y. Huang, K.-L. Wen, X.-J. Li, J.-J. Xie, C.-T. Chen, S.-C. Su, Coseismic deformation time history calculated from acceleration records using an EMD-derived baseline correction scheme: a new approach validated for the 2011 Tohoku Earthquake. Bull. Seismol. Soc. Am. **103**(2B), 1321–1335 (2013)
42. N.E. Huang, Z. Shen, S.R. Long, M.C. Wu, H.H. Shih, Q. Zheng, N-C Yen, C.C. Tung, and H.H. Liu. The empirical mode decomposition and the hilbert spectrum for nonlinear and non-stationary time series analysis. *Proceedings of the Royal Society of London. Series A: Mathematical, Physical and Engineering Sciences*, 454(1971):903–995, 1998
43. S. Huang, Z. Liu, Z. Liu, L. Wang, Sar image change detection algorithm based on different empirical mode decomposition. J. Comput. Commun. **5**, 9–20 (2017)
44. W. Huang, Z. Shen, N.E. Huang, Y.C. Fung, Use of intrinsic modes in biology: Examples of indicial response of pulmonary blood pressure to step hypoxia. Procee. Nat. Academy Sci. **95**(22), 12766–12771 (1998)
45. C.N. Jean, Y. Bouaoune, D. Eric, N. Oumar, P. Bunel, Image analysis by bidimensional empirical mode decomposition. Image Vision Comput. **21**, 1019–1026 (2003)
46. Tomasz Kalwarczyk, Natalia Ziebacz, Marcin Fialkowski, Robert Holyst, Late stage of the phase-separation process: Coalescence-induced coalescence, gravitational sedimentation, and collective evaporation mechanisms. Langmuir **24**(13), 6433–6440 (2008)
47. M. Kikuchi, Y. Okabe, A scaling approach to monte carlo renormalization group. Prog. Theo. Phys. **78**(3), 540–551 (1987)
48. Tiina Komulainen. Self-similarity and power laws. Technical report, Helsinki University of Technology, 2004
49. J.-M. Laherrère and P. Koutsikides. Alice, an instrument for the analysis of fluids close to the critical point in microgravity. *Acta Astronautica*, 29(10):861–870, 1993. World Space Congress
50. D. Liu, X. Chen, Image denoising based on improved bidimensional empirical mode decomposition thresholding technology. Multimedia Tools Appl. **78**, 7381–7417 (2018)
51. R. Marcout, J.F. Zwilling, J.M. Laherrere, Y. Garrabos, and Beysens D. ALICE 2, an advanced facility for the analysis of fluids close to their critical point in microgravity. In *45th Congress of the International Astronautical Federation, Jerusalem, Israel*. International Astronautical Federation, 1994
52. A. Moreno-Gomez, J.P. Amezquita-Sanchez, M. Valtierra-Rodriguez, C.A. Perez-Ramirez, A. Dominguez-Gonzalez, O. Chavez-Alegria, Emd-shannon entropy-based methodology to detect incipient damages in a truss structure. Appl. Sci. **8**(11), 2068 (2018)
53. J. Oh, J.M. Ortiz de Zárate, J.V. Sengers, G. Ahlers, Dynamics of fluctuations in a fluid below the onset of Rayleigh-Bénard convection. Phys. Rev. E **69**, 021106 (2004)
54. A. Oprisan, C. Garrabos, Y. Lecouter, D. Beysens, Measuring the transition rates of coalescence events during double phase separation in microgravity. Molecules **22**, 1125 (2017)
55. A. Oprisan, S.A. Oprisan, J.J. Hegseth, Y. Garrabos, C. Lecoutre-Chabot, D. Beysens, Universality in early-stage growth of phase-separating domains near the critical point. Phys. Rev. E **77**(5 Pt 1), 051118 (2008)
56. A. Oprisan, S.A. Oprisan, B. Bayley, J.J. Hegseth, Y. Garrabos, C. Lecoutre-Chabot, D. Beysens, Dynamic structure factor of density fluctuations from direct imaging very near (both above and below) the critical point of SF_6. Phys. Rev. E **86**, 061501 (2012)
57. A. Oprisan, S.A. Oprisan, J.J. Hegseth, C. Garrabos, Y. Lecouter, D. Beysens, Dimple coalescence and liquid droplets distributions during phase separation in a pure fluid under microgravity. Eur. Phys. J. E **37**, 1–10 (2014)
58. A. Oprisan, S.A. Oprisan, J.J. Hegseth, C. Garrabos, Y. Lecouter, D. Beysens, Direct imaging of long-range concentration fluctuations in a ternary mixture. Eur. Phys. J. E **38**, 1–9 (2015)
59. Ana Oprisan, Brittany Bayley, Sorinel A. Oprisan, John J. Hegseth, Yves Garrabos, Carole Lecoutre, and Daniel Beysens. Thermal fluctuation exponents for two near-critical point systems. In Zia ur Rahman,

Uncorrected Proof

Stephen E. Reichenbach, and Mark A. Neifeld, editors, *Visual Information Processing XIX*, volume 7701, pages 220 – 229. International Society for Optics and Photonics, SPIE, 2010

60. Ana Oprisan, Yves Garrabos, Carole Lecoutre-Chabot, Daniel Beysens, Multiscale empirical mode decomposition of density fluctuation images very near above and below the critical point of sf6. Physica A: Stat. Mech. Appl. **561**, 125293 (2021)
61. J.M. Ortiz de Zarate, C. Giraudet, H. Bataller, and F. Croccolo. Non-equilibrium fluctuations induced by the Soret effect in a ternary mixture. *The European Physical Journal E: Soft Matter*, 37:34, 08 2014
62. N. Otsu, A threshold selection method from gray-level histograms. IEEE Trans. Syst. Man Cybern. **9**(1), 62–66 (1979)
63. V. Pareto. *Cours d'Economie Politique Professe a l'Universite de Lausanne*. F. Rouge, 1897
64. S.T.G. Raghukanth, S. Sangeetha, Empirical mode decomposition of earthquake accelerograms. Adv. Adapt. Data Anal. **04**(04), 1250022 (2012)
65. G. Rilling, P. Flandrin, P. Goncalves, J.M. Lilly, Bivariate empirical mode decomposition. IEEE Signal Process. Lett. **14**(12), 936–939 (2007)
66. C. Sagui, M. Grant, Theory of nucleation and growth during phase separation. Phys. Rev. E **59**(4), 4175 (1999)
67. C. Sagui, D.S. O'Gorman, M. Grant, Nucleation, growth and coarsening in phase-separating systems. Scan. Microsc. **12**(1), 3–8 (1998)
68. A. Saha, M. Pukhrambam, S.N. Pradhan, Facial image analysis for expression recognition by bidimensional empirical mode decomposition. Indian J. Sci. Technol. **9**(31), 1–9 (2016)
69. N.A. Salingaros, B.J. West, A universal rule for the distribution of sizes. Environ. Plan. B: Plan. Design **26**(6), 909–923 (1999)
70. Helmut Satz, Cluster percolation and thermal critical behavior. Comput. Phys. Commun. **147**(1), 46–51 (2002)
71. R.E. Seoud, J.C. Vassilicos, Dissipation and decay of fractal-generated turbulence. Phys. Fluids **19**(10), 105108 (2007)
72. H. Song, H. Bai, L. Pinheiro, C. Dong, C.-Y. Huang, B. Liu, Analysis of ocean internal waves imaged by multichannel reflection seismics, using ensemble empirical mode decomposition. J. Geophys. Eng. **9**, 302–311 (2012)
73. Masuo Suzuki. Static and Dynamic Finite-Size Scaling Theory Based on the Renormalization Group Approach. *Progress of Theoretical Physics*, 58(4):1142–1150, 10 1977
74. Masuo Suzuki. Phase Transition and Fractals. *Progress of Theoretical Physics*, 69(1):65–76, 01 1983
75. A. Vailati, R. Cerbino, S. Mazzoni, C.J. Takacs, D.S. Cannell, M. Giglio, Fractal fronts of diffusion in microgravity. Nat. Commun. **2**(290), 1–5 (2011)
76. A. Vailati, M. Giglio, Nonequilibrium fluctuations in time-dependent diffusion processes. Phys. Rev. E **58**, 4361–4371 (1998)
77. Alberto Vailati, Marzio Giglio, Giant fluctuations in a free diffusion process. Nature **390**(6657), 262–265 (1997)
78. B. Widom, Intermolecular forces and the nature of the liquid state. Science **157**(3787), 375–382 (1967)
79. S. Will, A. Leipertz, Mutual diffusion coefficient and dynamic viscosity near the critical consolute point probed by dynamic light scattering. Int. J. Thermophys. **20**(3), 791–803 (1999)
80. Kenneth G. Wilson. Renormalization group and critical phenomena. i. renormalization group and the kadanoff scaling picture. *Phys. Rev. B*, 4:3174–3183, Nov 1971
81. Kenneth G. Wilson and Michael E. Fisher. Critical exponents in 3.99 dimensions. *Phys. Rev. Lett.*, 28:240–243, Jan 1972
82. Y. Xu, B. Liu, J. Liu, S. Riemenschneider, Two-dimensional empirical mode decomposition by finite elements. Procee. Royal Soc. A: Math. Phys. Eng. Sci. **462**(2074), 3081–3096 (2006)
83. Shunsuke Yabunaka, Akira Onuki, Critical adsorption profiles around a sphere and a cylinder in a fluid at criticality: Local functional theory. Phys. Rev. E **96**, 032127 (2017)
84. J. Zheng, J. Cheng, Y. Yang, Generalized empirical mode decomposition and its applications to rolling element bearing fault diagnosis. Mech. Syst. Signal Process. **40**(1), 136–153 (2013)
85. J. Zheng, H. Pan, S. Yang, J. Cheng, Generalized composite multiscale permutation entropy and laplacian score based rolling bearing fault diagnosis. Mech. Syst. Signal Process. **99**, 229–243 (2018)

uncorrected proof